frontiers

A radiative transfer simulator for PACE: theory and applications

Pengwang Zhai[1*], Meng Gao[2, 3], Bryan Franz[2], P. Jeremy Werdell[2], Amir Ibrahim[2], Yongxiang Hu[4], Jacek Chowdhary[5]

[1]Department of Physics, University of Maryland Baltimore County, Maryland, USA.

[2]Ocean Ecology Laboratory - Code 616, NASA Goddard Space Flight Center, Greenbelt, Maryland 20771, USA

[3]Science Systems and Applications, Inc., Greenbelt, MD, USA

[4]MS 475, NASA Langley Research Center, Hampton, VA 23681-2199, USA

[5]NASA Goddard Institute for Space Studies, New York, NY 10025, USA

*** Correspondence:**
Corresponding Author
pwzhai@umbc.edu

Keywords: PACE, radiative transfer, ocean color, ultraviolet, CDOM, brown carbon aerosols

Abstract

A radiative transfer simulator was developed to compute the synthetic data of all three instruments onboard NASA's Plankton Aerosol, Cloud, ocean Ecosystem (PACE) observatory, at the top of the atmosphere (TOA). The instrument suite includes the ocean color instrument (OCI), the Hyper-Angular Rainbow Polarimeter 2 (HARP2), and the Spectro-Polarimeter for Planetary Exploration 1 (SPEXone). The PACE simulator is wrapped around a monochromatic radiative transfer model based on the successive order of scattering (RTSOS), which accounts for atmosphere and ocean coupling, polarization, and gas absorption. Inelastic scattering, including Raman scattering from pure ocean water, fluorescence due to chlorophyll, and colored dissolved organic matter (CDOM), is also simulated. This PACE simulator can be used to explore the sensitivity of the hyperspectral and polarized reflectance of the Earth system with tunable atmosphere and ocean parameters, which include aerosol and cloud number concentration, refractive indices, and size distribution, ocean particle microphysical parameters, and solar and sensor-viewing geometry. The PACE simulator is used to study two important case studies. One is the impact of the significant uncertainty in pure ocean water absorption coefficient to the radiance field in the ultraviolet (UV) spectral region, which can be as much as 6%. The other is the influence of different amounts of brown carbon aerosols and CDOM on the polarized radiance field at TOA. The percentage variation of the radiance field due to CDOM is mostly for wavelengths smaller than 600 nm, while brown aerosols affect the whole spectrum from 350 to 890 nm, primarily due to covaried soot aerosols. Both case studies are important for aerosol and ocean color remote sensing and have not been previously reported in the literature.

1 Introduction

NASA's Plankton, Aerosol, Cloud, ocean Ecosystem (PACE) mission will carry the Ocean Color Instrument (OCI), which is a hyperspectral scanning radiometer with spectral coverage from the ultraviolet (340 nm) to near-infrared (890 nm) measured at 5 nm spectral resolution with 2.5-nm spectral sampling (Werdell et al., 2019). The 5-nm resolution will better resolve spectral features of some plankton species, as well as atmospheric gas absorption features such as the Oxygen-A band centered near 765 nm. OCI also includes seven shortwave infrared (SWIR) bands centered on 940, 1038, 1250, 1378, 1615, 2130, and 2260 nm, to be used for ocean color atmospheric correction and aerosol and cloud retrievals. In addition, PACE plans to carry two Multi-Angle Polarimeters (MAPs): the Hyper-Angular Rainbow Polarimeter 2 (HARP2) (McBride et al., 2020) and the Spectro-Polarimeter for Planetary Exploration 1 (SPEXone) (Hasekamp et al. 2019). HARP2 will measure the first three Stokes parameters (I, Q, U) at four wavelengths (441, 549, 669, 873 nm) and at multiple viewing angles (60 angles for 669 nm, and 10 angles for the other wavelengths) for each pixel. SPEXone will measure the radiance and the Degree of Linear Polarization (DoLP) from 385 to 770 nm with a variable spectral resolution of 2-5 nm for radiance and 10-40 nm for DoLP at five viewing angles, but with less swath coverage than OCI and HARP2. The combined dataset of OCI and the MAPs will provide a plethora of data that will significantly enhance our understanding of the Earth's ocean, atmosphere, and land systems.

Satellite sensors such as OCI, HARP2, and SPEXone measure radiometric signals at the top of the atmosphere (TOA). Remote sensing algorithms infer environmental variables from the radiometric signals. Over oceans, the environmental variables may include the abundance of aerosols, cloud particles, and hydrosols (in-water particles) and their microphysical properties, many of which are used to infer biogeophysical properties. The radiative transfer model governs the relationship between the environmental variables and radiometric signals, which use the single-scattering properties of particles as inputs. It is imperative to build a satellite sensor simulator based on rigorous radiative transfer models, which conserves the transfer of energy and adequately simulates the interactions between the light and the medium. Rigorous models would allow for understanding the change of radiometric signals in response to variations in the environmental variables needed for developing and testing remote sensing algorithms. The simulator also needs to account for the radiometric characteristics of the sensors, such as the spectral response, so that it can be used as the best representation of the sensor measurements, which maximizes the benefits of a satellite mission.

In this paper, we report a PACE simulator, which can simulate the hyperspectral radiance that OCI would measure and the polarized signals at multiple wavelengths and multiple viewing angles from HARP2 and SPEXone. The simulator is built around a vector radiative transfer model, which models light multiply scattered in the coupled atmosphere-ocean systems based on the successive order of scattering method (Zhai et al., 2009, 2010). Plane-parallel geometry is assumed in the radiative transfer model, i.e., we only consider the vertical variation of the optical properties of the atmosphere and ocean. Scattering and absorption due to molecules, aerosols, clouds, and oceanic particles are accurately considered. Gas absorption due to H_2O, CO_2, O_2, CH_4, O_3, and NO_2 are adequately accounted for, which is essential for studying the photon path length distribution in the strong absorbing bands. The model can also simulate inelastic scattering in ocean waters, i.e., Raman scattering by pure waters and fluorescence due to chlorophyll and colored dissolved organic matter (CDOM) (Zhai et al., 2015, 2017). The detailed system configuration and algorithm are described in Sec. 2.

Previously, the Global Ocean Physical-Biogeochemical Model (Gregg and Rousseaux, 2017) was developed, which can generate a proxy of global distributions of spectral water leaving radiances based on the spatial distribution of ocean components from the global ocean circulation model. As a

result, approximations have been used in the radiative transfer process in the ocean. Our simulator aims to represent all properties of the radiation field in both the atmosphere and ocean as accurately as possible, which preserves both the angular dependence of the light field and the polarization properties.

Two applications of the PACE simulator are presented in the result section. One is a sensitivity study on the impacts of the uncertainty of the spectral absorption coefficient of pure seawater in the ultraviolet (UV) on the radiance field at TOA. The absorption coefficient of pure seawater in the UV is poorly characterized, with values that vary by two orders of magnitude within the literature (Lee et al., 2015; Mason et al., 2016; Twardowski et al., 2018). This uncertainty will significantly impact ocean color remote sensing in the UV once the OCI data is available. The other study is on the convoluted influences of aerosols and CDOM on both radiance and degree of linear polarization at TOA. In particular, both brown carbon and CDOM spectral absorption coefficients increase exponentially as wavelength decreases in the UV. The similarity of the spectral variation of these two components of the atmosphere and ocean system has created great challenges in quantifying their abundances. This paper reports our sensitivity study on different amounts of brown carbon aerosols (Mok et al., 2016) as well as CDOM (Twardowski, 2004) to the radiance field using our new PACE simulator, which is a novel contribution to the remote sensing field.

This paper is organized as the following: Sec. 2 describes the theoretical background of the various elements of this PACE simulator; Sec. 3 covers the two sensitivity studies in the UV we performed using the PACE simulator; Sec. 4 provides the discussion.

2 Theoretical background

2.1 Atmospheric and ocean optical properties

2.1.1 Atmospheric components

The description of radiative transfer processes in the atmosphere needs vertical profiles of scattering and absorbing particles to be properly defined as inputs. The atmospheric particles include molecules, as well as aerosol and cloud particles. The default profiles of molecules in the PACE simulator are based upon the US standard atmosphere (1976), but other profiles can easily be substituted by using input files with the same data format. The profile data include the total number density of atmospheric molecules and the volume mixing ratios of the significant absorbers (H_2O, CO_2, O_2, CH_4, O_3, and NO_2) in the UV-SWIR spectral range. The scattering cross-section and the depolarization ratio are a function of wavelength, temperature, and pressure, which we calculate using the algorithm of Tomasi (2005). The molecular scattering cross-section is multiplied by the total number density and integrated over height to obtain the optical depths due to molecular scattering in each discretized vertical layer. We use the Rayleigh scattering matrix, which depends on the depolarization ratio for characterizing molecular scattering (Hovenier et al., 2004).

The scattering matrices of aerosols or clouds can be calculated by the Mie theory for spherical particles (Mishchenko et al., 2002) or other more flexible methods for non-spherical particles, for instance, the finite-difference time-domain method (Yang and Liou, 1996; Sun et al., 2017), the T-matrix method (Mishchenko et al., 2002; Bi and Yang, 2014), and discrete dipole approximation (Yurkin and Hoekstra, 2011). The scattering matrices from different components (molecules, aerosols, and cloud particles) can be weighted by their scattering optical depth in a discretized vertical layer, i.e.:

$$\mathbf{P_t}(\Theta) = \left(\tau_{s,m}\mathbf{P_m}(\Theta) + \tau_{s,a}\mathbf{P_a}(\Theta) + \tau_{s,c}\mathbf{P_c}(\Theta)\right)/\left(\tau_{s,m} + \tau_{s,a} + \tau_{s,c}\right) \quad (1)$$

where $\mathbf{P_t}(\Theta)$, $\mathbf{P_m}(\Theta)$, $\mathbf{P_a}(\Theta)$, and $\mathbf{P_c}(\Theta)$ are the scattering matrices for molecules, aerosols, and cloud particles, respectively, as a function of scattering angle Θ; and $\tau_{s,m}$, $\tau_{s,a}$, and $\tau_{s,c}$ are the scattering optical depths for molecules, aerosols, and clouds, respectively. The scattering optical depth τ_s for a vertical layer bounded by heights z_0 and z_1 are calculated by:

$$\tau_s = \int_{z_0}^{z_1} C_{scat}(z)n(z)dz \quad (2)$$

where C_{scat} is the scattering cross section and $n(z)$ is the number density of particles in consideration. The number density $n(z)$ from Braslau and Dave (1973) are used as the default vertical distribution of aerosols, though it can be easily changed.

The extinction optical depth τ_e can be calculated in the same way as Eq. (2) by replacing C_{scat} by C_{ext} which is the extinction cross-section. The single scattering albedo for a layer is defined as:

$$\omega = \left(\tau_{s,m} + \tau_{s,a} + \tau_{s,c}\right)/\left(\tau_{s,m} + \tau_g + \tau_{e,a} + \tau_{e,c}\right) \quad (3)$$

where τ_g, $\tau_{e,a}$, and $\tau_{e,c}$ are the optical depth due to gas absorption, aerosol extinction, and cloud extinction, respectively.

The gas absorption optical depth τ_g is calculated from the absorption cross-section of a gas molecule, the number density, and its vertical distribution. The ARTS software (Buehler et al., 2018) is used to generate the absorption cross-section look-up-table for H_2O, CO_2, O_2, and CH_4 based on the molecular parameters from the HITRAN database (Gordon et al., 2017). The ozone and NO_2 absorption sections are interpolated from the data from Serdyuchenko et al. (2014) and Burrows et al. (1998), respectively.

2.1.2 Ocean components

The ocean is bounded by the air-sea interface, with its surface roughness parameterized in terms of wind speed (Cox and Munk, 1954). The ocean body is assumed to be a mixture of pure seawater, phytoplankton particles and their derivative non-algal particles, and CDOM. The Einstein–Smoluchowski phase function is adopted to represent scattering by pure seawater (Mobley, 1994). The scattering coefficient of seawater is a function of salinity and temperature based on Zhang and Hu (2009). In this paper we have used the salinity of 37‰ and temperature of 20℃. The absorption coefficients in the visible, namely $\lambda \geq 550$ nm, are from the measurements by Pope and Fry (1997). In the UV there is no consensus on the magnitude of the absorption coefficient of pure water yet. We consider three sources in this paper: the International Ocean Colour Coordinating Group (IOCCG) protocol, which compiles several credible data (Twardowski et al., 2018, hereafter referred to as IOC), the best possible retrieval data by Lee et al. (2015, hereafter referred to as LEE) based on in-water radiometric measurements, and pure water absorption data measured by Mason et al. (2016, hereafter referred to as MCF).

Figure 1 shows the absorption coefficient from the three sources between 300 to 550 nm. MCF is smaller than both IOC and LEE, especially in the UV. The shortest wavelength in the LEE dataset is 350 nm, below which we use the same values as in IOC. The large discrepancy we see in Fig. 1 imposes significant uncertainties in ocean color remote sensing in the UV. Sec. 3 reports a sensitivity study of

the TOA radiance due to this discrepancy, which helps quantify the error in future remote sensing algorithms of ocean color in the UV.

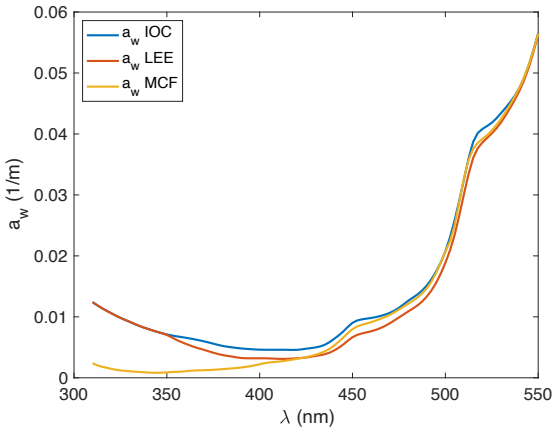

Figure 1. The absorption coefficients of pure water from the three sources: IOC, LEE, and MCF.

The spectral absorption coefficient $a_p(\lambda)$ of the total particulate matter is parameterized in terms of chlorophyll-a concentration [Chla]:

$$a_p(\lambda) = A_p(\lambda)[\text{Chla}]^{E_p(\lambda)} \tag{4}$$

where A_p and E_p are the coefficients from Bricaud et al. (1998). The data from Bricaud et al. (1998) covers the wavelength from 400-700 nm. For λ<400 nm, another source of data from Bricaud et al. (2010) is used to expand the spectral range to the UV. The absorption coefficient in λ<400 nm is scaled to ensure continuity between these two datasets at 400 nm.

The spectral backscattering coefficient $b_{bp}(\lambda)$ is modeled by (Morel and Maritorena, 2001, IOCCG, 2006 and reference within):

$$b_{bp}(\lambda) = b_{bp}(660)(660/\lambda)^{S_{bp}} \tag{5}$$

where the free parameter $b_{bp}(660)$ is the backscattering coefficient for phytoplankton particles at 660 nm and S_{bp} is the spectral exponent. The backscattering fraction B_{bp} can be modeled as a spectrally flat constant (Whitmire et al. 2007) so that $b_p(\lambda) = b_{bp}(\lambda)/B_{bp}$. The extinction coefficient is the sum of absorption and scattering coefficients: $c_p(\lambda) = a_p(\lambda) + b_p(\lambda)$.

Another option to parameterize $c_p(\lambda)$ is to make it a power law function of wavelength (Voss, 1992) and model the scattering coefficients as $b_p(\lambda) = c_p(\lambda) - a_p(\lambda)$, which can be easily adopted in the simulator by switching an internal logical flag. We did not use this option in the sensitivity presented in Sec. 3.

The phase function of the phytoplankton particle is determined by the backscattering fraction B_{bp} based on Mobley et al. (1993). The total phase function of ocean water is:

$$\mathrm{P}_t(\Theta) = \left(b_w \mathrm{P}_w(\Theta) + b_p \mathrm{P}_p(\Theta)\right)/\left(b_w + b_p\right) \tag{6}$$

where b_w and $\mathrm{P}_w(\Theta)$ are the scattering coefficient and phase function of the pure sea water; and $\mathrm{P}_p(\Theta)$ is the phase function of phytoplankton particles determined by B_{bp}. The scattering matrix of ocean water is:

$$\mathbf{P}_t(\Theta) = \mathrm{P}_t(\Theta)\bar{\mathbf{M}}(\Theta) \tag{7}$$

where $\bar{\mathbf{M}}$ is the reduced Mueller matrix of ocean waters measured by Voss and Fry (1984).

CDOM in our model is assumed to be absorbing only, i.e., the scattering coefficient of CDOM is zero. The absorbing coefficient of CDOM is modeled as:

$$a_{CDOM}(\lambda) = \Phi a_{CDOM}(\lambda_{ref}) \exp\left[-S_{CDOM}(\lambda - \lambda_{ref})\right] \tag{8}$$

where Φ is a constant factor to account for natural variability of ocean waters (Morel et al. 2009). In Morel and Gentili (2009), the reference wavelength is $\lambda_{ref} = 400$ nm; $a_{CDOM}(400) = 0.065[\mathrm{Chla}]^{0.63}$; and $S_{CDOM} = 0.018$ nm^{-1}. This option represents the global ocean average, which is referred to as MG2009. In Morel et al. (2007), $\lambda_{ref} = 370$ nm; $a_{CDOM}(370) = 0.1[\mathrm{Chla}]^{0.8}$; and $S_{CDOM} = 0.016$ nm^{-1}, which is referred to as MAG2007 representing the behavior of south pacific oceans.

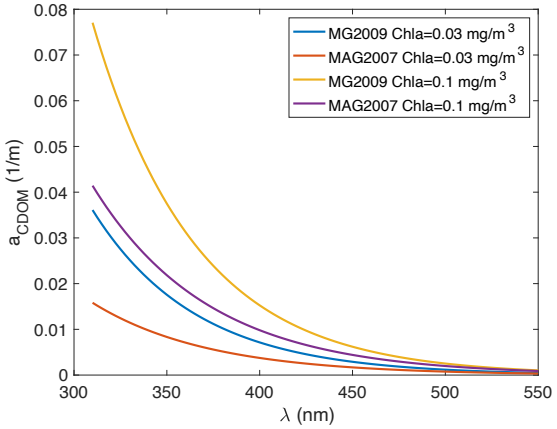

Figure 2. The absorption coefficient of CDOM as a function of wavelength for two [Chla] values: 0.03 mg/m^3 and 0.3 mg/m^3. Φ=1 in Eq. (8) is used in the figure.

Figure 2 shows the CDOM absorption coefficients as a function of wavelength for [Chla] = 0.03 mg/m^3 and [Chla] =0.1 mg/m^3 calculated by using MG2009 and MAG2007 with $\Phi = 1$. The MAG2007 values are much lower than those from MG2009 for the same [Chla] value, which we will use in our sensitivity study in Sec. 3.

We also have an option to include the scattering and absorption by sediments following Ibrahim et al. (2016) and Zhai et al. (2017), which we will not emphasize in this paper.

2.2 Monochromatic vector radiative transfer model (RTSOS)

The core of the PACE simulator is a monochromatic radiative transfer model based on the successive order of scattering method (RTSOS) (Zhai et al., 2009, 2010). This model was recently validated in a comprehensive comparison and testbed study (Chowdhary et al., 2020). The atmospheric and ocean

optical properties as a function of wavelength is provided as input to RTSOS to calculate the polarized radiance field at user specified locations. The total radiance field is denoted by $\mathbf{L}_t = (I, Q, U, V)^T$, where I, Q, U, and V are the Stokes parameters and the superscript T stands for matrix transpose. In RTSOS, $\mathbf{L}_t$ is decomposed into contributions from different orders of scattering $\mathbf{L}_n$:

$$\mathbf{L}_t(\lambda, \theta_s, \theta_v, \phi_v) = \sum_{n=1}^{N} \mathbf{L}_n(\lambda, \theta_s, \theta_v, \phi_v) \quad (9)$$

where N is the maximum order of scattering included in the series, θ_s is the solar zenith angle, and θ_v and ϕ_v are the viewing zenith and azimuth angles, respectively. Note that we define $\phi_v = 0$ as the half plane where the sun glint is located in, so that the azimuth angle of the solar ray is always zero. The first order of scattering solution $\mathbf{L}_1$ can be solved analytically in the atmospheric and ocean system (Zhai et al., 2012), and each higher-order scattering solution can be obtained by performing optical depth and solid angle integrations of the previous order solution (Zhai et al., 2010).

For the scattering functions with a large forward peak, we implemented several truncation methods to increase the efficiency and maintain the accuracy, including the Delta-M method (Wiscombe, 1977), δ-fit method (Hu et al., 2000), and Delta-M+ method (Lin et al., 2018). The default option is the δ-fit method, which gives the best solution in most of the situations. RTSOS solves the vector radiative transfer equation at viewing angles corresponding to discrete Gaussian quadrature points. An advanced interpolation scheme based on the integration of source function is used to obtain the radiance field at arbitrary viewing angles (Zhai et al. 2013).

To simulate inelastic scattering processes in ocean waters, the excitation radiation field is obtained by looping elastic RTSOS over the excitation wavelengths to evaluate the inelastic source function at the emission wavelength (Zhai et al., 2015, 2017). The chlorophyll fluorescence quenching processes can be modeled by allowing the quantum yield, and the fraction of photons reemitted in the total number of photons absorbed by chlorophyll molecules, to vary with the instantaneous photosynthetically available radiation (IPAR) (Morrison and Goodwin, 2010). For more details on how inelastic scattering is implemented in the radiative transfer model, readers are referred to Zhai et al. (2015, 2017).

2.3 Double-k method for simulating intra-band spectral response

The PACE simulator calls RTSOS in each instrument channel to simulate the radiance field at the center wavelength at a specified location and viewing direction. For channels with little or weak gas absorption, an averaged gas absorption optical depth $\bar{\tau}_g$ can be calculated for each atmospheric layer:

$$T(\lambda_i) = \int_{-\infty}^{\infty} \exp\left[-\tau_g(\lambda)\right] \mathrm{ILS}(\lambda_i, \lambda) d\lambda \,/\, \int_{-\infty}^{\infty} \mathrm{ILS}(\lambda_i, \lambda) d\lambda \quad (10)$$

$$\bar{\tau}_g(\lambda_i) = -\ln[T(\lambda_i)] \quad (11)$$

where λ_i is the center wavelength of ith channel; $\tau_g(\lambda)$ is the monochromatic optical depth at λ; and $\mathrm{ILS}(\lambda_i, \lambda)$ is the instrument line shape function for ith channel. Using $\bar{\tau}_g$, we only need to call RTSOS once for each channel to simulate the band averaged polarized radiance.

In some strong absorption bands of gases, such as the Oxygen-A band centered at 765 nm, the absorption cross-section can vary by several orders of magnitude within the full width at half maximum (FWHM) of the considered channel. The approximation made in Eqs. (10-11) will

introduce a significant error that cannot be tolerated. In this case, we adopt the philosophy of the double-k method (Duan et al., 2005) to model the monochromatic radiance in a channel by:

$$\mathbf{L}_t(\lambda) = \begin{cases} \mathbf{L}_c / \left[\tau_g(\lambda) - d\right]^e & \tau_g(\lambda) \in [0,1] \\ \mathbf{L}'_c \exp\left\{-\left[f \cdot \tau_g(\lambda)\right]\right\} & \tau_g(\lambda) \in (1,5] \\ \mathbf{L}''_c \exp\left\{-\left[h \cdot \tau_g(\lambda)\right]\right\} & \tau_g(\lambda) \in [5,\infty) \end{cases} \quad (12)$$

where $\mathbf{L}_c$, $\mathbf{L}'_c$, $\mathbf{L}''_c$, d, e, f, and h are fitting parameters. To find these fitting parameters, the PACE simulator calls RTSOS m times within $\left[\lambda_i - \frac{\text{FWHM}}{2}, \lambda_i + \frac{\text{FWHM}}{2}\right]$ for a channel centered at λ_i. The number of calls m depends on the maximum value of the gas absorption optical depth $\tau_{g,max}$, i.e., m=3 if $\tau_{g,max} < 1$; m=5 if $1 < \tau_{g,max} < 5$; m=7 if $\tau_{g,max} > 5$. The resultant radiance vectors are denoted as $\mathbf{L}_t(\lambda_i, \lambda_j)$, where $j = 1,2,\ldots,m$. The first three wavelengths $\lambda_{j=1,2,3}$ are sampled in $\tau_g(\lambda_j) \in [0,1]$; $\lambda_{j=4,5}$ are sampled in $\tau_g(\lambda_j) \in [1,5]$, and $\lambda_{j=6,7}$ are sampled in $\tau_g(\lambda_j) \in [5,10]$. In all three intervals $\ln \tau_g(\lambda_j)$ is uniformly distributed in $[\ln \tau'_{g,min}, \ln \tau'_{g,max}]$ where $\tau'_{g,max}$ and $\tau'_{g,min}$ are the maximum and minimum values in the gas absorption optical depth interval. If $\tau'_{g,max}$>10, we set $\tau'_{g,max} = 10$ to avoid unnecessary simulations of small reflectance. After the fitting parameters are found in Eq. (12), the band averaged radiance can be found with:

$$\mathbf{L}_t(\lambda_i) = \int_{\lambda_{min}}^{\lambda_{max}} \mathbf{L}_t(\lambda)\, \text{ILS}(\lambda_i, \lambda) d\lambda \quad (13a)$$

where the integration limit λ_{min} and λ_{max} are determined by the negligible values of $\text{ILS}(\lambda_i, \lambda)$. The integration can be numerically approximated by the following summation:

$$\mathbf{L}_t(\lambda_i) = \sum_k \mathbf{L}_t(\lambda_k)\, \text{ILS}(\lambda_i, \lambda_k) \Delta\lambda_k \quad (13b)$$

where $\lambda_k \in [\lambda_{min}, \lambda_{max}]$ is the discretized integration wavelength and the wavelength step $\Delta\lambda_k$ is small enough to resolve the spectral features of the gas absorbing bands. In the weakly absorbing bands, $\Delta\lambda_k$ is mostly 0.1 nm. In strongly absorbing bands, for instance, the oxygen A (~765 nm) and B (~686 nm) bands, $\Delta\lambda_k$ is as small as 0.005 nm. A sensitivity test (not shown) indicated that the fitting scheme Eq. (12-13) provides an accuracy level better than 0.5% for most OCI channels, which meets the calibration goal of OCI (Werdell et al., 2019). For a few strongly absorbing bands, including oxygen A and B bands, the error could be as large as 1%.

3 Simulation results

In this section we present two novel sensitivity studies to show the capabilities of our PACE simulator. The first one is the impact of the uncertainty of pure ocean water absorption coefficients on the radiance field at TOA. In ocean color remote sensing, this is the essential baseline knowledge needed before obtaining information on other constituents. As we showed in Sec. 2.1.2, there is a large discrepancy in pure water absorption coefficients in the UV. Understanding the variation of the TOA radiance field due to this uncertainty will help the remote sensing community better quantify and interpret derived biogeophysical and bio-optical products. In the second sensitivity study, we check the influences of different amounts of brown carbon aerosols in the atmosphere and CDOM in the ocean to the TOA polarized reflectance to explore how one can address the difficulty of separating the two signals. OCI and SPEXone will cover the UV spectral region, where both brown carbon aerosols and CDOM have increased absorption as wavelength decreases. Brown carbon

aerosols are essential for evaluating the radiative forcing balance in the Earth system, while CDOM is critical for ocean carbon cycle studies. It is important to separate two signals and quantify them.

3.1 Variation of the TOA radiance field due to the uncertainty of the pure water absorption coefficient in the UV

The PACE simulator is used to simulate the spectral TOA reflectance, $\rho_t(\lambda) = \pi L_t(\lambda)/E_d(\lambda)$, where $L_t(\lambda)$ and $E_d(\lambda)$ are the upwelling radiance and the downwelling irradiance at TOA, respectively. The molecular density is from the 1976 US standard atmosphere. The aerosol model is the Urban aerosol model from Shettle and Fenn (1976) with the relative humidity of 0.90. The aerosol optical depth at 550 nm is 0.1. In the ocean, three sources of the absorption coefficient of the pure ocean water are used: IOC (Twardowski et al., 2018), LEE (Lee et al., 2015), and MCF (Mason et al., 2016). Two [Chla] values are used: 0.03 mg/m^3 and 0.1 mg/m^3. For each [Chla] value, two CDOM absorption bio-optical models are used to see the impacts of different waters: MG2009 and MAG2007. Other inherent optical properties are the same as those outlined in Sec. 2.1.2. No sediment is included in the simulation. Ocean water depth is set as 200 meters so that the bottom effect is minimal at TOA. The solar zenith angle is 30 degrees.

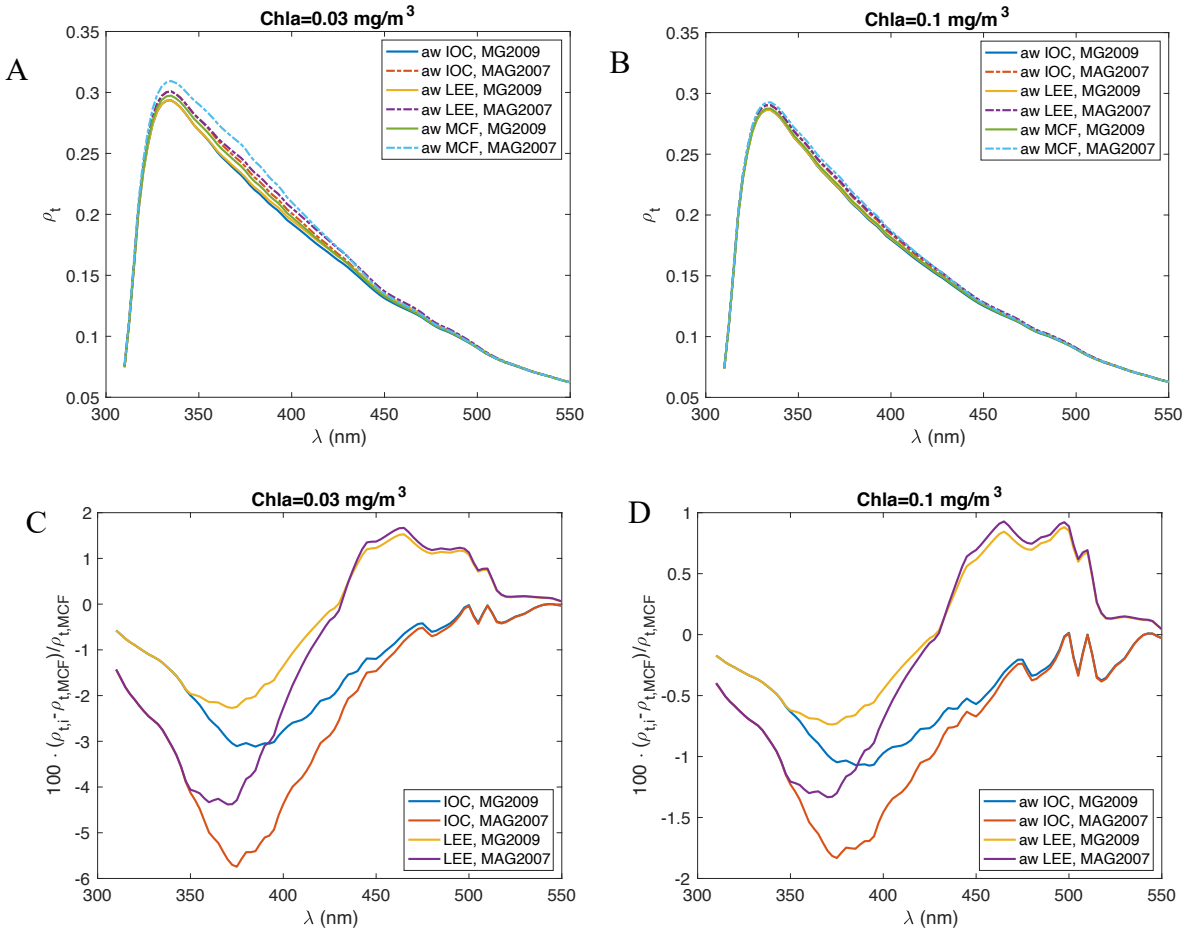

Figure 3. (A) the total reflectance at TOA for [Chla]=0.03 mg/m^3. Six curves are shown, corresponding to three sources of water absorption coefficients times two different CDOM absorption parameterization in [Chla]. (B) the same as Fig. 3(A), except for [Chla]=0.1 mg/m^3. (C) the percentage difference of the TOA reflectance compared to MCF, where the subscript i in $\rho_{t,i}$ can be either IOC or LEE, as shown in the legend. (D) the same as (C) except for [Chla]=0.1 mg/m^3.

Figures 3(A) and 3(B) show the TOA reflectance at nadir as a function of wavelength for [Chla]=0.03 mg/m^3 and 0.1 mg/m^3, respectively. FWHM of 5 nm is used in the simulation. Figure 3(C) shows the percentage differences of the reflectances calculated with LEE and IOC with respect to those with MCF for [Chla]=0.03 mg/m^3. Figure 3(D) is the same as Fig. 3(C) except for [Chla]=0.1 mg/m^3. It can be seen that the impact of the different a_w values is larger when [Chla] is small (0.03 mg/m^3), which is expected because the contribution of a_w in the total absorption coefficient becomes smaller when [Chla] becomes larger, as both a_p and a_{CDOM} increase with [Chla] in the UV. Figures (C-D) show that adopting MAG2007 leads to a larger percentage difference between different a_w data, as a_{CDOM}based on MAG2007 is smaller than those of MG2009 so that the relative importance of a_w is larger. Overall, the impacts of different a_w source are in the range of -6%–2% for [Chla]=0.03 mg/m^3 and -2%–1% for [Chla]=0.1 mg/m^3, respectively. This is small albeit detectable by OCI, whose calibration accuracy is 0.5%. In ocean color remote sensing the water leaving contribution is mostly smaller than 10% of the total signal at TOA at 440 nm. The uncertainty of the TOA reflectance would be amplified some 10 times in terms of the accuracy of the water leaving signals, which becomes worse in the UV due to large atmospheric signal contribution.

3.2 Impacts of brown carbon aerosols and CDOM to the polarized radiance field at TOA

We used the PACE simulator to simulate polarized reflectance at the TOA for nine cases with different amounts of brown aerosol and CDOM in the coupled atmosphere and ocean system. The wind speed is 5 m/s. The ocean water is assumed to be a mixture of pure seawater, phytoplankton particles, and CDOM. The absorption coefficient of the phytoplankton particles follows the bio-optical model Eq. (4) with [Chla]=1 mg/m^3. The backscattering coefficient at 660 nm $b_{bp}(660)$ is 0.00347 m^{-1}; the spectral exponent S_{bp} is 0.15 nm^{-1}; and the backscattering fraction B_{bp} is 0.01 and has no spectral dependence (Whitmire et al. 2007). This leads to $b_p(660) = 0.347$ m^{-1} which is consistent with Morel and Maritorena (2001) when [Chla]= 1 mg/m^3. For the absorption coefficient of CDOM, we use reference wavelength of λ_{ref}=440 nm, and $a_{CDOM}(440)$= 0.0316 m^{-1} and $S_{cdom} = 0.018$ nm^{-1}, which are calculated by MG2009 with [Chla]=1 mg/m^3. In addition, we perturb the CDOM absorption by setting $\Phi = 0.5$ and 2 in Eq. (8) so that two more values of $a_{CDOM}(440)$ are used: 0.0158 and 0.0632 m^{-1}, which creates a variability of a_{CDOM} so that it can be compared with the effect of variable amounts of absorbing aerosols.

The aerosol optical depth is 0.1 at 550 nm. The aerosol model is assumed to be a bio-modal lognormal distribution, with the fine and coarse modes to be 90% and 10% of the total volume, respectively. The coarse mode is assumed to be sea salt with the effective radius and variance of 2.0194 μm and 0.672, respectively. The fine mode is assumed to be an internal mixture of dust-like, water-soluble, and brown carbon, and soot carbon aerosols, with the effective radius and variance of 0.15 μm and 0.437, respectively. Three brown carbon volume fractions are used in the fine mode: 0.02, 0.04, and 0.06 (Schuster et al., 2016, Shi et al., 2020). The volume ratio of dust-like to water-soluble aerosols is fixed at 1:3, while the volume ratio of brown carbon to soot carbon aerosols is assumed to be 2, which is consistent with Schuster et al. (2016). If brown carbon aerosol fraction in the fine mode is 0.02, the corresponding soot, dust-like, and water soluble aerosol volume fraction are: 0.01, (1-0.02-0.01)/4=0.2425, (1-0.02-0.01)·3/4=0.7275, respectively. These numbers will need to be multiplied by 90% to get their total fraction in aerosols including both fine and coarse modes. The fractions of the different components of the other two cases can be calculated similarly, with the fractions showing in Table 1.

Table 1. The volume fractions of different components for the aerosol models used in the study.

Aerosol Models	Fine Mode (0.90)				Coarse Mode
	Brown Carbon	Soot Carbon	Water Soluble	Dust-like	
BrC Frac 0.02	0.02 × 0.9 = 0.018	0.01 × 0.9 = 0.009	0.7275 × 0.9 = 0.6548	0.2425 × 0.9 = 0.2182	Sea Salt (0.10)
BrC Frac 0.04	0.04 × 0.9 = 0.036	0.02 × 0.9 = 0.018	0.7050 × 0.9 = 0.6345	0.2350 × 0.9 = 0.2115	Sea Salt (0.10)
BrC Frac 0.06	0.06 × 0.9 = 0.054	0.03 × 0.9 = 0.027	0.6825× 0.9 = 0.6142	0.2275 × 0.9 = 0.2048	Sea Salt (0.10)

The refractive indices of soot carbon, dust-like, water-soluble, and sea-salt are from Shettle and Fenn (1979). The real refractive index n of brown carbon is set to 1.55 for all wavelengths and the imaginary part k between 375 nm and 532 nm is based on the Kramers-Kronig fitting of the measurement data from Sumlin et al. (2018). For $\lambda < 375$ nm, we use the exponent fitting (Mok et al., 2016):

$$k(\lambda) = k(375)\left(\frac{375}{\lambda}\right)^{5.7} \tag{14}$$

where $k(375) = 0.01235$ is from Sumlin et al. (2018) to ensure continuity.

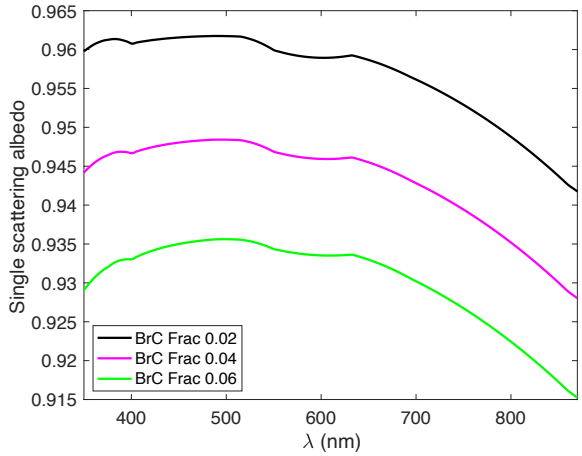

Fig. 4. The single scattering albedo of the three aerosol models with the brown carbon volume factions of 0.02, 0.04, and 0.06 in the fine mode.

Figure 4 shows the singe scattering albedo of the aerosol models with three different brown carbon volume fractions: 0.02, 0.04, and 0.06 in the fine mode. It shows that the single scattering albedo ranges between 0.915 and 0.965. It is smaller for smaller brown carbon fraction, primarily due to soot carbon which is ½ of brown carbon volume fraction. The separation between the three lines in the

370 UV bands are slightly larger than other spectral region, indicating the influence of brown carbon. In
371 addition, the DoLP signal has different sensitivity to single scattering albedo, which may be used to
372 further differentiate the influence of CDOM and absorbing aerosols.

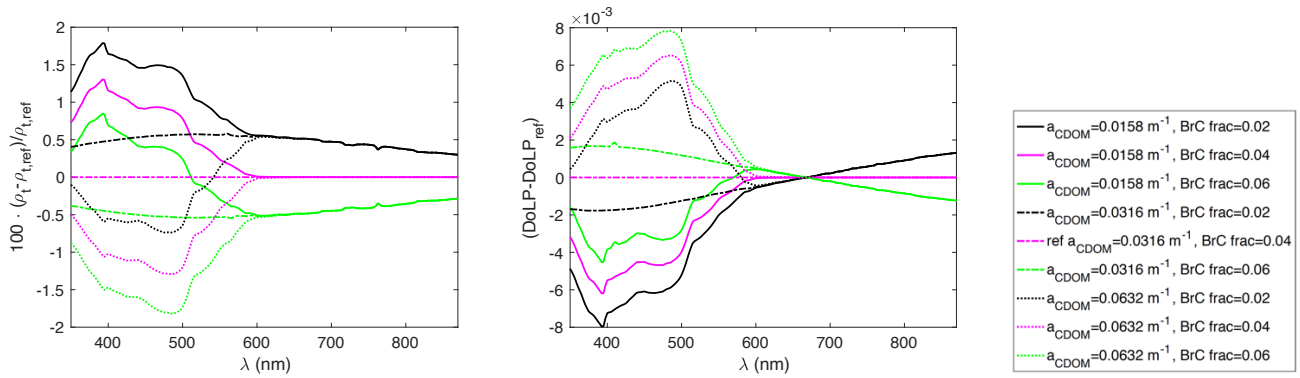

373

374 Fig. 5. Left: the percentage difference of the TOA reflectance with respect to a reference case (ref),
375 which corresponds to $a_{CDOM}(440) = 0.0316$ m^{-1} and the brown carbon aerosol fraction of 0.04, i.e.,
376 the dash magenta color line. Right: the absolute difference of the TOA DoLP with respect to the
377 reference case (ref).

378 We calculate the percentage difference of the TOA signals for each case in comparison to a reference
379 case, which is $a_{CDOM}(440) = 0.0316$ m^{-1} and the brown carbon aerosol fraction of 0.04. The left
380 and right diagrams of Fig. 5 show the variation of the TOA reflectance and degree of linear
381 polarization (DoLP), respectively. The solar zenith angle is 30 degrees and the viewing angle is set to
382 be 60 degrees with the relative azimuth angle of 0 degrees, which is in the same half-plane as the
383 glint. The influence of different $a_{CDOM}(440)$ values is mainly for wavelength shorter than 600 nm,
384 while the different values of brown carbon fractions move the reflectance up and down in the whole
385 spectral range. The DoLP plot shows different trends from those of reflectance, which can be used to
386 enhance the accuracy of the retrieval algorithms. The calibration requirement of OCI is 0.5%, which
387 is sufficient to discriminate the variation shown in Fig. 5. The polarization signal variation is between
388 -0.008 to 0.008, which can be detected by SPEXone, which aims to achieve 0.003 of DoLP accuracy
389 (Werdell et al., 2019).

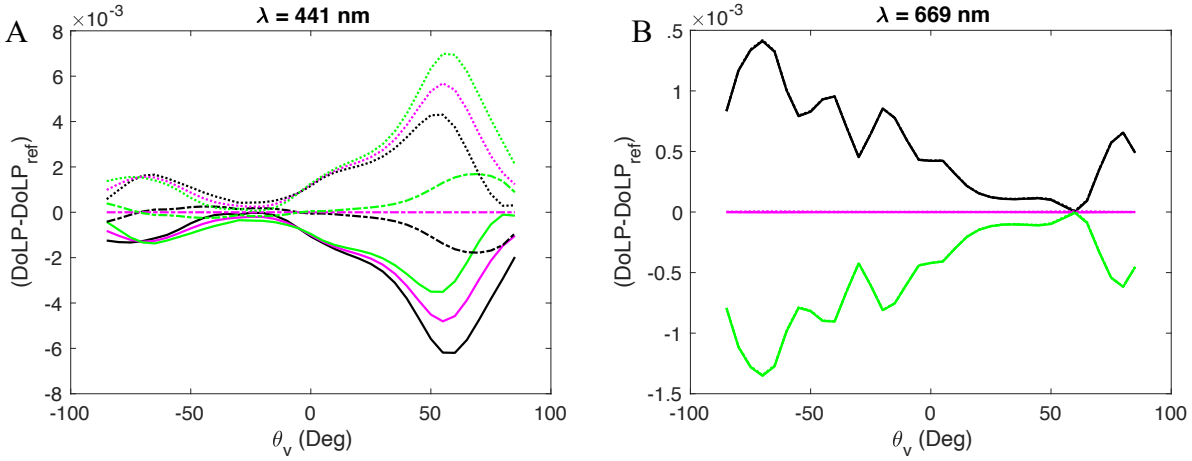

390

391 Fig. 6. (A) DoLP-DoLP$_{ref}$ in the principal plane as a function of viewing zenith angle at 441 nm,
392 where ref is corresponds to the case of $a_{CDOM}(440) = 0.0316$ m^{-1} and the brown carbon aerosol

fraction of 0.04. (B) the same as (A) except for the wavelength of 669 nm. The figure legend is the same as Fig. 5.

The MAP instruments will measure the polarized radiance at different viewing angles, which can provide extra information on the aerosol and hydrosol microphysics. Fig. 6 shows the dependence of DoLP in the principal plane as a function of viewing zenith angle. The principal plane is defined as the plane containing the direct solar ray and local vertical. Positive viewing zenith angles indicate the half plane with an azimuth angle of 0 degrees, which contains the sun glint, while negative viewing zenith angles are the half plane of an azimuth angle of 180 degrees. Two HARP wavelengths, 441 and 669 nm, are chosen to show the angular dependence. At 441 nm, both the brown carbon fractions and the CDOM absorption coefficients have visible influences on the DoLP at TOA (see Fig. 6(A), the difference of DoLP with those of a reference case). At 669 nm, the influence due to CDOM absorption diminishes and only brown carbon aerosols would have influences on DoLP. The DoLP change at 441 nm is as large as 0.008. It is smaller at 669 nm for which the DoLP change is mostly smaller than 0.00015, which is hard to be differentiated by SPEXone. The angular dependence of DoLP at TOA at different wavelength can be used to differentiate the brown carbon fraction and CDOM absorption if a proper data fitting algorithm is implemented.

4 Discussion

In this paper, we described a PACE simulator that is built upon rigorous radiative transfer models. The monochromatic radiative transfer model is based on the successive order of scattering method for coupled atmosphere and ocean systems. A series of periphery software packages were developed to set up the atmospheric and ocean optical properties as a function of wavelengths. In the atmosphere, the Rayleigh scattering matrix is used for molecular scattering, with the scattering cross-section and depolarization factor calculated based on the atmosphere's vertical pressure and temperature profiles. The aerosol and cloud properties can be flexibly set. A number of commonly used aerosol models are built in the simulator for the convenience of users, including Shettle and Fenn (1979) and Ahmad et al. (2010) . Gas absorptions are considered by using a hyperspectral gas absorption cross-section look-up-table calculated with the HITRAN database and a few other suitable sources. In the ocean, a number of different bio-optical models are included to model the scattering and absorption of light by various components, including pure seawater, phytoplankton and their derivative non-algal particles, and CDOM. The model can use chlorophyll-a concentration as a sole parameter to parameterize the ocean water inherent optical properties, which represent the behaviors of open ocean waters. It can provide a number of options where the inherent optical properties of different components do not follow the global average behavior so that we can model the coastal and inland waters. Inelastic scattering of ocean waters, including Raman scattering, fluorescence due to chlorophyll and CDOM can be modeled. All three PACE instruments, OCI, HARP, and SPEXone, are considered. The PACE simulator generates the Stokes parameters (I, Q, U, V) for a sensor at arbitrary locations in the atmosphere and ocean.

To show an application of the PACE simulator, we present two sensitivity studies in the UV. One is the variation of the TOA radiance field due to the uncertainty of the pure ocean water absorption coefficient. There are some large differences in pure water absorption coefficients in the UV among different sources. We choose the three most credible sources, and their differences are as large as a couple of orders of magnitude. Using a typical setting of the atmosphere and ocean system, we found that the variation of the TOA radiance field is largest for smaller chlorophyll concentrations, which ranges between -6% – 2% for [Chla]=0.03 mg/m^3 at different wavelengths. For [Chla]=0.1 mg/m^3, the difference reduces to -2% – 1%. In the second study, we present the influence of different brown

carbon fraction and CDOM amount to the polarized radiance field at TOA. We found that the influence of CDOM on the reflectance is for wavelengths smaller than 600 nm, while brown carbon affects the whole spectrum, primarily due to covaried soot aerosols. The polarized signal has a different spectral trend from the reflectance. The angular dependence of DoLP at 441 nm is sensitive to both brown carbon fractions and the CDOM absorption, while the influence of CDOM is minimal at 669 nm. The percentage difference between the different values of the brown carbon fraction (0.02, 0.04, and 0.06) is of the order of 1-2%, which can be detected by the OCI instrument, whose goal is to achieve 0.5% calibration accuracy. The DoLP variation is around 0.008, which can also be detected by SPEXone whose DoLP accuracy requirement is 0.003. These properties can be used to design remote sensing algorithms which retrieve the brown carbon and CDOM abundance.

In summary, our PACE simulator can be used in a wide range of applications, including sensitivity studies of different atmosphere and ocean components, the generation of synthetic data for testing remote sensing algorithms, and building look-up tables for atmospheric correction of ocean color remote sensing.

5 Conflict of Interest

The authors declare that the research was conducted in the absence of any commercial or financial relationships that could be construed as a potential conflict of interest.

6 Author Contributions

PZ and YH developed the original radiative transfer concept. PZ implemented the simulation algorithm and generated the sensitivity study. BF and MG advised on the PACE instrument characteristics. PJW and AI provided bio-optical model used in the simulator. PJW advised on the ocean water absorption sensitivity study. YH provided advice on the data analysis. JC suggested on brown carbon microphysical properties. All authors contributed to the editing of the manuscript.

7 Funding

This research is partially supported by NASA grants 80NSSC20M0227 and 80NSSC18K0345.

8 Acknowledgments

References

Ahmad, Z., B. A. Franz, C. R. McClain, E. J. Kwiatkowska, J. Werdell, E. P. Shettle, and B. N. Holben, (2010), New aerosol models for the retrieval of aerosol optical thickness and normalized water-leaving radiances from the SeaWiFS and MODIS sensors over coastal regions and open oceans, Appl. Opt. 49, 5545-5560.

Bi, L., and Yang, P. (2014). Accurate simulation of the optical properties of atmospheric ice crystals with invariant imbedding T-matrix method. J. Quant. Spectrosc. Radiat. Transfer, 138, 17–35.

Braslau, N. and J. V. Dave, (1973), Effect of Aerosols on the Transfer of Solar Energy Through Realistic Model Atmospheres. Part I: Non-Absorbing Aerosols, J. Appl. Meteor. 12, 601-615.

Bricaud, A., Morel, A., Babin, M., Allali, K., and Claustre, H. (1998). Variations of light absorption by suspended particles with chlorophyll a concentration in oceanic (case 1) waters: analysis and implications for bio-optical models. J. Geophys. Res. 103, 31033–31044.

Bricaud, A., Babin, M., Claustre, H., Ras, J., and Tièche, F. (2010) Light absorption properties and absorption budget of Southeast Pacific waters, J. Geophys. Res. 115, C08009.

Buehler, S. A., Mendrok, J., Eriksson, P., Perrin, A., Larsson, R., and Lemke O. (2018) ARTS, the atmospheric radiative transfer simulator -- version 2.2, the planetary toolbox edition, Geosci. Model Dev., 11(4), 1537–1556, doi:10.5194/gmd-11-1537-2018.

Burrows, J. P., Dehn, A., Deters B., Himmelmann S., Richter., A., Voigt S., Orphal J. (1998) Atmospheric remote-sensing reference data from GOME: 1. Temperature-dependent absorption cross sections of NO2 in the 231–794 nm range. J. Quant. Spectrosc. Radiat. Transf. 60, 1025–31.

Chowdhary, J., Zhai, P., Xu, F., Frouin, R., and Ramon, D., (2020) Testbed results for scalar and vector radiative transfer computations of light in atmosphere-ocean systems. *J. Quant. Spectrosc. Radiat. Transfer*, **242**, 106717.

Cox, C. and W. Munk (1954). Measurement of the roughness of the sea surface from photographs of the suns glitter, J. Opt. Soc. Am., 44, 838-850.

Duan, M., Min, Q., and Li, J. (2005), A fast radiative transfer model for simulating high-resolution absorption bands, J. Geophys. Res., 110, D15201, doi:10.1029/2004JD005590.

Gordon, I.E., Rothman, L.S., Hill, C., et al., (2017). The HITRAN2016 Molecular Spectroscopic Database, J. Quant. Spectrosc. Radiat. Transf. 203, 3-69.

Gregg, W.W., and Rousseaux, C.S. (2017). Simulating PACE global ocean radiances. Frontiers in Marine Science 4: 1-19. doi:10.3389/fmars.2017.00060

Hasekamp, O. P., Fu, G., Rusli, S. P., Wu, L., Di Noia, A., de Brugh, J., et al. (2019). Aerosol measurements by SPEXone on the NASA PACE mission: expected retrieval capabilities. J. Quant. Spectrosc. Radiat. Transf. 227, 170–184. doi: 10.1016/j.jqsrt.2019.02.006.

Hovenier, J. W., Van Der Mee, C., and Domke, H., (2004) Transfer of polarized light in planetary atmospheres: basic concepts and practical methods, vol. 318. doi:10.1007/978-1-4020-2856-4.

Hu, Y., Wielicki, B., Lin, B., Gibson, G., Tsay, S. -C., Stamnes, K., and Wong, T. (2000) δ -Fit: A fast and accurate treatment of particle scattering phase functions with weighted singular-value decomposition least-squares fitting. J. Quant. Spectrosc. Radiat. Transfer 65, 681–690.

Ibrahim, A., Gilerson, A., Chowdhary, J., and Ahmed, S. (2016). Retrieval of macro- and micro-physical properties of oceanic hydrosols from polarimetric observations, Rem. Sens. Environ. 186, 548–566.

IOCCG (2006). Remote Sensing of Inherent Optical Properties: Fundamentals, Tests of Algorithms, and Applications. Lee, Z.-P. (ed.), Reports of the International Ocean-Colour Coordinating Group, No. 5, IOCCG, Dartmouth, Canada.

Lee, Z., Wei, J., Voss, K., Lewis, M., Bricaud, A., and Huot, Y. (2015). Hyperspectral absorption coefficient of “pure” seawater in the range of 350-550 nm inverted from remote sensing reflectance. Appl. Opt. 54, 546-558.

514 Lin, Z., Chen, N., Fan, Y., Li, W., Stamnes, K., & Stamnes, S. (2018). New Treatment of Strongly
515 Anisotropic Scattering Phase Functions: The Delta-M+ Method, Journal of the Atmospheric
516 Sciences, 75(1), 327-336.

517 Mason, J. D., Cone, M. T., and Fry, E. S., (2016). Ultraviolet (250–550 nm) absorption spectrum of
518 pure water, Appl. Opt. 55, 7163-7172.

519 McBride, B. A., Martins, J. V., Barbosa, H. M. J., Birmingham, W., and Remer, L. A., (2020). Spatial
520 distribution of cloud droplet size properties from Airborne Hyper-Angular Rainbow Polarimeter
521 (AirHARP) measurements, Atmos. Meas. Tech., 13, 1777–1796, https://doi.org/10.5194/amt-13-
522 1777-2020.

523 Mishchenko, M. I., Travis, L. D., and Lacis, A. A. (2002). Scattering, Absorption, and Emission of
524 Light by Small Particles. Cambridge University Press, Cambridge.

525 Mobley, C. D., Gentili, B., Gordon, H. R., Jin, Z., Kattawar, G. W., Morel, A., Reinersman, P.,
526 Stamnes, K., and Stavn, R. H. (1993). Comparison of numerical models for computing
527 underwater light fields, Appl. Opt. 32, 7484–7504.

528 Mobley CD. (1994) Light and water: radiative transfer in natural waters. San Diego, CA: Academic
529 Press.

530 Mok, J., Krotkov, N., Arola, A. et al. (2016). Impacts of brown carbon from biomass burning on
531 surface UV and ozone photochemistry in the Amazon Basin. Sci Rep 6, 36940.
532 https://doi.org/10.1038/srep36940.

533 Morel, A., and Maritorena, S. (2001), Bio-optical properties of oceanic waters: A reappraisal, J.
534 Geophys. Res., 106(C4), 7163– 7180, doi:10.1029/2000JC000319.

535 Morel, A., Claustre, H., Antoine, D., and Gentili, B. (2007). Natural variability of bio-optical
536 properties in Case 1 waters: attenuation and reflectance within the visible and near-UV spectral
537 domains, as observed in South Pacific and Mediterranean waters, Biogeosciences, 4, 913–925,
538 https://doi.org/10.5194/bg-4-913-2007.

539 Morel, A., and Gentili B. (2009). A simple band ratio technique to quantify the colored dissolved and
540 detrital organic material from ocean color remotely sensed data, Rem. Sens. Environ., 113, 998-
541 1011.

542 Morrison, R.J., Goodwin, D.S. (2010). Phytoplankton photocompensation from space based
543 fluorescence measurements. Geophys. Res. Lett. 37.

544 Pope, R. M., and Fry, E. S. (1997) Absorption spectrum (380–700 nm) of pure water. II Integrating
545 measurements, Appl. Opt. 36, 8710–8723.

546 Serdyuchenko, A., Gorshelev, V., Weber, M., Chehade, W., and Burrows, J. P. (2014). High spectral
547 resolution ozone absorption cross-sections – Part 2: Temperature dependence, Atmos. Meas.
548 Tech., 7, 625–636, https://doi.org/10.5194/amt-7-625-2014.

549 Shettle, E. P., and Fenn, R. W. (1979) Models for the aerosols of the lower atmosphere and the e
550 ects of humidity variations on their optical properties, AFGL-TR-79-0214 U.S. Air Force
551 Geophysics Laboratory, Hanscom Air Force Base, Mass..

552 Sumlin, B. J., Heinson, Y. W., Shetty, N., Pandey, A., Pattison, R. S., Baker, S., Hao, W. M.,
553 Chakrabarty, R. K. (2018). UV–Vis–IR spectral complex refractive indices and optical properties
554 of brown carbon aerosol from biomass burning, J. Quant. Spectrosc. Radiat. Transf. 206, 392-
555 398. https://doi.org/10.1016/j.jqsrt.2017.12.009.

Tomasi, C., Vitale, V., Petkov, B., Lupi, A., and Cacciari A. (2005). Improved algorithm for calculations of Rayleigh-scattering optical depth in standard atmospheres. Appl. Opt., 44, 3320-3341.

Twardowski, M.S., Boss, E., Sullivan, J.M., and Donaghay, P.L. (2004). Modeling the spectral shape of absorption by chromophoric dissolved organic matter. Marine Chemistry, 89: 69-88.

Twardowski, M., Röttgers, R., and Stramski, D. (2018) Chapter 1: The Absorption Coefficient, An Overview, in Inherent Optical Property Measurements and Protocols: Absorption Coefficient, edited by A.R. Neeley and A. Mannino, IOCCG Ocean Optics and Biogeochemistry Protocols for Satellite Ocean Colour Sensor Validation, Volume 1.0, IOCCG, Dartmouth, NS, Canada.

U.S. Standard Atmosphere, 1976, U.S. Government Printing Office, Washington, D.C., 1976. https://ccmc.gsfc.nasa.gov/modelweb/atmos/us_standard.html

Schuster, G. L., Dubovik, O., and Arola, A.: Remote sensing of soot carbon – Part 1: Distinguishing different absorbing aerosol species, Atmos. Chem. Phys., 16, 1565–1585, https://doi.org/10.5194/acp-16-1565-2016, 2016.

Shi, C., M. Hashimoto, K. Shiomi, and T. Nakajima, 2021: Development of an Algorithm to Retrieve Aerosol Optical Properties Over Water Using an Artificial Neural Network Radiative Transfer Scheme: First Result From GOSAT-2/CAI-2. IEEE Transactions on Geoscience and Remote Sensing. 59, 9861-9872, doi: 10.1109/TGRS.2020.3038892.

Sun, W., Hu Y., Weimer, C., Ayers, K., Baize, R., Lee, T., (2017). A FDTD solution of scattering of laser beam with orbital angular momentum by dielectric particles: Far-field characteristics, J. Quant. Spectrosc. Radiat. Transfer, 188, 200-213, doi:10.1016/j.jqsrt.2016.02.006.

Voss, K. J., and Fry, E. S. (1984). Measurement of the Mueller matrix for ocean water, Appl Opt. 23, 4427–4439.

Voss, K.J. (1992). A spectral model of the beam attenuation coefficient in the ocean and coastal areas. Limnol. Oceanogr., 37, 501–509.

Werdell, P.J., Behrenfeld, M.J., Bontempi, P.S., Boss, E., Cairns, B., Davis, G.T., Franz, B.A., Gliese, U.B., Gorman, E.T., Hasekamp, O., Knobelspiesse, K.D., Mannino, A., Martins, J.V., McClain, C.R., Meister, G., and Remer, L.A. (2019). The Plankton, Aerosol, Cloud, Ocean Ecosystem Mission: Status, Science, Advances, Bull. Am. Meteorol. Soc., 100(9), doi: 10.1175/BAMS-D-18-0056.1.

Whitmire, A. L., Boss, E., Cowles, T. J., and Pegau, W. S., (2007) Spectral variability of the particulate backscattering ratio, Opt. Express 15, 7019-7031.

Wiscombe, W. J. (1977) The Delta-M method: rapid yet accurate radiative flux calculations for strongly asymmetric phase functions. J. Atmos. Sci. 34, 1408–1422.

Yang P., and Liou, K. N. (1996) Finite-difference time domain method for light scattering by small ice crystals in three-dimensional space, J. Opt. Soc. Am. A 13, 2072-2085.

Yurkin M.A. and Hoekstra A.G. (2011). The discrete-dipole-approximation code ADDA: capabilities and known limitations, J. Quant. Spectrosc. Radiat. Transfer 112, 2234–2247.

Zhai, P., Hu, Y., Trepte, C. R., and Lucker, P. L. (2009). A vector radiative transfer model for coupled atmosphere and ocean systems based on successive order of scattering method. Opt. Express 17, 2057-2079.

Zhai, P., Hu, Y., Chowdhary, J., Trepte, C. R., Lucker, P. L., and Josset, D. B. (2010). A vector radiative transfer model for coupled atmosphere and ocean systems with a rough interface. J. Quant. Spectrosc. Radiat. Transfer, 111, 1025-1040.

Zhai, P., Hu, Y., Josset, D. B., Trepte, C. R., Lucker, P. L., and Lin, B. (2012) Exact first order scattering correction for vector radiative transfer in coupled atmosphere and ocean systems, in Polarization: Measurement, Analysis, and Remote Sensing X, vol. 8364. doi:10.1117/12.920767.

Zhai, P., Hu, Y., Josset, D. B., Trepte, C. R., Lucker, P. L., and Lin, B., (2013). Advanced angular interpolation in the vector radiative transfer for coupled atmosphere and ocean systems. J. Quant. Spectrosc. Radiat. Transfer, 115, 19–27. doi:10.1016/j.jqsrt.2012.09.018.

Zhai, P., Hu, Y., Winker, D. M., Franz, B., Boss, E., (2015). Contribution of Raman scattering to polarized radiation field in ocean waters, Opt. Express, 23(18), 23582-23596.

Zhai, P., Hu, Y., Winker, D. M., Franz, B., Werdell, J.,Boss, E., (2017). A vector radiative transfer model for coupled atmosphere and ocean systems including inelastic sources in ocean waters, Opt. Express, Opt. Express 25, A223-A239.

Zhai, P., Knobelspiesse, K., Ibrahim, A., Franz, B. A., Hu, Y., Gao, M., and Frouin, R. (2017) Water-leaving contribution to polarized radiation field over ocean. Opt. Express 25, A689-A708.

Zhai, P., Boss, E., Franz, B., Werdell, P. J., Hu, Y., (2018) Radiative Transfer Modeling of Phytoplankton Fluorescence Quenching Processes. Remote Sens., 10, 1309. https://doi.org/10.3390/rs10081309.

Zhang, X. and Hu, L. (2009) Scattering by pure seawater at high salinity, Opt. Express 17, 12685–12691.